Journal of Materials Chemistry B

ROYAL SOCIETY OF CHEMISTRY

PAPER

View Article Online
View Journal | View Issue



Cite this: J. Mater. Chem. B, 2020, 8, 8294

# Biocide mechanism of highly efficient and stable antimicrobial surfaces based on zinc oxide–reduced graphene oxide photocatalytic coatings†

Laura Valenzuela,*[a] Ana Iglesias-Juez,*[b] Belén Bachiller-Baeza,[b] Marisol Faraldos,[b] Ana Bahamonde[b] and Roberto Rosal[a]

Received 5th June 2020,
Accepted 21st July 2020

DOI: 10.1039/d0tb01428a

rsc.li/materials-b

Highly efficient photoactive antimicrobial coatings were obtained using zinc oxide–reduced graphene oxide nanocomposites (ZnO–rGO). Their remarkable antibacterial activity and high stability demonstrated their potential use for photoactive biocide surfaces. The ZnO–rGO nanocomposites were prepared by the sol–gel technique to create photocatalytic surfaces by spin-coating. The coatings were deeply characterised and several tests were performed to assess the antibacterial mechanisms. rGO was homogeneously distributed as thin sheets decorated with ZnO nanoparticles. The surface roughness and the hydrophobicity increased with the incorporation of graphene. The ZnO–rGO coatings exhibited high activity against the Gram-positive bacterium *Staphylococcus aureus*. The 1 wt% rGO coated surfaces showed the highest antibacterial effect in only a few minutes of illumination with up to 5-log reduction in colony forming units, which remained essentially free of bacterial colonization and biofilm formation. We demonstrated that these coatings impaired the bacterial cells due to cell membrane damage and intracellular oxidative stress produced by the photogenerated reactive-oxygen species (ROS). The enhancement of the ZnO photocatalytic performance upon rGO incorporation is due to the increased detected generation of hydroxyl radicals, attributed to the reduction of electron–hole pair recombination. This intimate contact between both components also conveyed stability against zinc leaching and improved the coating adhesion.



## Introduction

In recent decades, microbial contamination and biofilm formation have become severe concerns in many fields, ranging from healthcare to industrial environments, due to the increased bacterial resistance to antibiotics.[1–3] Consequently, the development of alternative bactericidal strategies based on nanotechnology has aroused significant interest.[4] Photocatalytic antimicrobial coatings involving metal oxide nanoparticles represent an emerging approach in order to inactivate a wide variety of microorganisms, and prevent transmission and infection problems.[5] Among inorganic semiconductors, ZnO is one of the most promising photocatalysts owing to its natural abundance, low cost, non-toxicity, chemical stability, tunable nanometric architecture, wide band-gap (3.37 eV) and large exciton binding energy (60 meV).[6,7] Moreover, ZnO displays antimicrobial activity against different microorganisms even in the dark mainly due to the generation of reactive oxygen species (ROS) and the release of zinc ions.[8–10] However, the recombination rate of the photogenerated electron–hole pairs decreases its photocatalytic performance, thus limiting its practical application.[11]

Graphene (or reduced graphene oxide), a two-dimensional layer structure of $sp^2$-hybridized carbon atoms, has emerged as a new functional material for many technological applications due to its large surface area, high electrical conductivity, superior mechanical properties and biocompatibility.[12–14] These unique properties make graphene an excellent electron-transport material in photocatalysis, suppressing charge carrier recombination.[15–18] Graphene oxide (GO) contains a series of reactive oxygen functional groups (including carboxylic acids and hydroxyl groups), which provide possible sites for interaction with metal or metal oxide particles.[19,20] Therefore, GO can be used as a precursor material to anchor semiconductor particles, followed by the subsequent reduction of GO to rGO to obtain composites with intimate interfacial contact.[21–26]

Besides, the deposition technique selected to fabricate the nanostructured coating can influence the thickness and the

[a] Department of Chemical Engineering, University of Alcalá, E-28871 Alcalá de Henares, Madrid, Spain
[b] Instituto de Catálisis y Petroleoquímica, ICP-CSIC, Marie Curie 2, 28049 Madrid, Spain. E-mail: ana.iglesias@icp.csic.es

† Electronic supplementary information (ESI) available. See DOI: 10.1039/d0tb01428a

surface roughness.[27] Spin-coating is a simple technique for obtaining uniform layers on relatively flat surfaces.[28] Alternative techniques such as spray-coating, electrochemical deposition or electrospray have multiple coupled variables, making process optimization more complex.[29] In the spin-coating process, the film thickness and morphology can be modulated by depositing successive layers of coating and selecting the appropriate rotation speed.[30,31] Fast operation, cost-effectiveness and good repeatability are additional advantages of this procedure.[32]

The aim of this work was to combine the remarkable electrical and mechanical properties of rGO with the high antibacterial performance of ZnO nanoparticles to prepare improved photoactive bactericidal surfaces by a spin-coating technique using a sol–gel preparation method. The bioactivity of the ZnO–rGO nanocomposites with different rGO loadings was assayed against a Gram-positive pathogenic bacterium, *Staphylococcus aureus*. The coatings were deeply characterised and several tests were performed to assess the charge transfer processes and antibacterial mechanisms. Since good performance should also include resistance and reuse after washing the coating, it is important to evaluate the reusability of the photocatalytic coatings by assaying the same coatings under repeated incubation–irradiation cycles.

This complete approach allowed us to identify the active species and establish the action mechanism of these surfaces that presented great biocide and stability properties, which shows their great potential for coating functional surfaces.

## Experimental

### Fabrication and characterisation of photocatalytic surfaces

Zinc oxide nanoparticles were prepared by sol–gel synthesis based on an version of the method reported by Spanhel and Anderson and described in detail in our previous work.[33,34] Briefly, 0.14 M zinc acetate dehydrate $Zn(CH_3COO)_2{\cdot}2H_2O$ was dissolved in methanol ($CH_3OH$), by magnetically stirring for 1 hour at room temperature. Then, 0.14 M tetramethylammonium hydroxide ($(CH_3)_4NOH$), 25 wt% in methanol, was added drop wise. After aging for 48 hours, a stable ZnO suspension was obtained and used for coating without any post-conditioning. An appropriate amount of graphene oxide (GO, Graphenea, Spain) was ultrasonically dispersed in the ZnO sol and stirred overnight in order to obtain nanocomposites with 0.5, 1.0 and 1.5 wt% GO, relative to ZnO. The resultant suspensions were deposited on glass substrates ($1 \times 1$ cm$^2$ approx.), by the spin-coating technique (WS-650-23B, Laurell Technologies Corporation). Prior to the deposition process, the substrates were sequentially cleaned in an ultrasonic bath with detergent, distilled water, acetone, ethanol and distilled water, and then dried at 150 °C for 10 minutes. The spin-coating process was carried out *via* dynamic dispensing at 500 rpm for 0.2 seconds followed by 15 seconds of acceleration and drying steps at 1500 and 3500 rpm, respectively. After spin-coating, the samples were dried at 150 °C for 10 minutes to evaporate the residual solvent and the procedure was repeated ten times, achieving a mass surface density of $0.11 \pm 0.05$ mg cm$^{-2}$. Finally, the coated specimens were calcined in air at 300 °C (to achieve complete GO deoxygenation) for 1 hour to obtain the ZnO–rGO nanocomposite films, which were denoted as ZnO–0.5rGO, ZnO–1.0rGO and ZnO–1.5rGO, respectively.

The crystal structure of the as-prepared films was characterised by X-ray diffraction (PANalyticalX'Pert Pro) using $CuK_\alpha$ radiation. The diffraction patterns were recorded within Bragg's angles ranging from 2° to 90°, with 0.04° step and 50 s per point. Phase identification and their distribution on the coatings were addressed by Raman maps of the functionalised surfaces recorded on a Renishaw Qontor-Raman spectrometer using a 405 nm laser and a 2400 grating. The mapping area on the optical microscopy images (100× magnification) corresponds to a grid surface of 40 nm × 55 nm, with 3 nm *X* and *Y* step sizes (285 scans) and a spectral acquisition of one accumulation and 3 s. The morphology of the fabricated films was investigated by scanning electron microscopy (SEM, Zeiss DSM 950) and transmission electron microscopy (TEM/STEM, JEOL 2100F) at an accelerating voltage of 25 and 200 kV, respectively. The surface roughness was measured using a phenom scanning electron microscope equipped with 3D Roughness Reconstruction software (cut-off, $\lambda_c = 77.88$ μm; shortwave profile filter, $\lambda_s = 344$ nm). The optical properties of the samples were analysed by UV-vis diffuse reflectance spectroscopy (DRS) using Agilent Cary 5000 equipment. The photoluminescence (PL) spectra of the photocatalytic coatings were recorded by using a LS50B Perking Elmer luminescence spectrometer at an excitation wavelength of 350 nm. The wettability of the spin-coated surfaces was evaluated by measuring the water contact angle (WCA) using the sessile drop technique (DSA25, Krüss).

### Antimicrobial activity assays and bioanalytical procedures

The antibacterial properties of the ZnO and ZnO–rGO photocatalytic surfaces were evaluated using a biofilm-forming Gram-positive bacterium *Staphylococcus aureus* (CECT 240) by using the aerosol spraying exposure methodology. The microorganism growth was conducted using nutrient broth (NB, 5 g L$^{-1}$ beef extract, 10 g L$^{-1}$ peptone, 5 g L$^{-1}$ NaCl, pH $7.0 \pm 0.2$) at 37 °C under agitation. 7 μL cm$^{-2}$ of a suspension of $10^8$ cell mL$^{-1}$ were sprayed with a nebulizer on functionalised and non-functionalised glass substrates in a sealed polypropylene chamber.[32] Specimens were incubated for 20 hours in the dark at 37 °C and at a relative humidity above 96%, which was achieved using a hygrostatic $K_2SO_4$ solution following the recommendation OIML R 121.[35]

The bacteria-colonized samples were irradiated with a 365 nm UV light source (LED BLS 13000-1, Mightex). The lamp was adjusted to simulate Winter–Fall, L(+), and Summer–Spring, L(++), daylight exposure conditions. The NASA Surface Meteorology and Solar Energy Database (https://power.larc.nasa.gov/) indicated that the average daily incident insolation was 6.1 and 2.7 kW h m$^{-2}$ in Summer–Spring and Winter–Fall, respectively, for the latitude of Madrid. The irradiation time was regulated to irradiate with one third of the reported values as a conservative assumption, meaning 2.0 kW h m$^{-2}$ for Summer–Spring and 1.0 kW h m$^{-2}$

for Winter–Fall, that is 6 and 3 minutes, respectively. The fact that only 5.2% and 5.7% of Summer–Spring and Winter–Fall irradiation correspond to UV irradiation was also considered.

The number of viable cells adhering to the surfaces was determined by plate counting according to the standard ISO 22196. Briefly, the specimens were transferred to 24-well plates first containing PBS (phosphate buffered saline) for 15 minutes to remove non-adhered bacteria and subsequently SCDLP broth (Soybean casein digest broth with lecithin and polyoxyethylene sorbitan monooleate) for 30 minutes to recover those attached to the surface. 10 μL spots of 10-fold serial dilutions of SCDLP in PBS were placed on agar plates (2.5 g $L^{-1}$ yeast extract, 5 g $L^{-1}$ tryptone, 1 g $L^{-1}$ glucose, 15 g $L^{-1}$ agar powder) and incubated at 37 °C for 24 hours. The number of colony forming units (CFUs) provided considers at least three replicates of at least two serial dilutions.

The cell viability as a function of the membrane integrity was assessed using a live/dead Baclight Bacterial Viability Kit (Fisher Scientific). 10 μL per sample of an appropriate mixture of green-fluorescent SYTO 9 and red-fluorescent propidium iodide (PI) stain in DMSO (according to the manufacturer's recommendations) were used followed by 15 minutes of incubation in the dark at room temperature. SYTO 9 labels all bacteria, whereas PI penetrates only cells with disrupted membranes. The excitation/emission wavelengths were 488/500–575 and 561/570–620 nm for green and red fluorescence, respectively. FilmTracer SYPRO Ruby (Fisher Scientific) was used to visualize the biofilm matrix. Briefly, 200 μL of FilmTracer stain were added to each specimen followed by 30 minutes of incubation in the dark at room temperature. The biofilm was observed using confocal microscopy (Leica TCS-SP5) excitation at 450 and emission at 610 nm.

The generation of hydroxyl radicals ($HO^{\bullet}$) under UV light irradiation at the photocatalytic coating surface was investigated using terephthalic acid (TA) as a probe molecule.[36,37] Non-fluorescent TA reacts with $HO^{\bullet}$ to produce a highly fluorescent product, 2-hydroxyterephthalic acid (HTA), and therefore the fluorescent intensity is proportional to the $HO^{\bullet}$ amount produced during the photocatalytic process. The coatings were immersed in 2.5 mL $cm^{-2}$ solution of 0.5 mM terephthalic acid and 2 mM NaOH. After 30 minutes in the dark, to reach the adsorption–desorption equilibrium, the coatings were illuminated with UV light for *in situ* $HO^{\bullet}$ generation. Then, the fluorescence intensity generated by HTA was measured using 200 μL of solution in contact with the functionalised and non-functionalised surfaces in black 96-well plates and excitation and emission wavelengths of 360 and 460 nm were used, respectively.

Intracellular oxidative stress was assessed using dichlorofluorescein (DCF) as an indicator. 2′,7′-Dichlorodihydrofluorescein diacetate ($H_2$DCFDA) easily penetrates the bacterial cell membrane. After entry into the cytoplasm, $H_2$DCFDA is intracellularly hydrolyzed to form the dichlorodihydrofluorescein carboxylate anion, which is oxidized by hydrogen peroxide and other ROS to the fluorescent DCF.[38,39] To perform the test, coated and uncoated surfaces were colonized with bacteria following the same procedure as explained above. After incubation and UV irradiation, 50 μL of 10 mM $H_2$DCFDA in DMSO were added to the surfaces placed on a flat black plate. The plate was incubated at 25 °C for 1 hour and the surface fluorescence was measured with a fluorometer (Fluoroskan Ascent FL, Thermo Scientific) with excitation and emission wavelengths of 485 and 538 nm, respectively.

To assess the stability and possible release of $Zn^{2+}$ ions from the ZnO and ZnO–rGO functionalised surfaces, the coated substrates were submerged in water (2.5 mL $cm^{-2}$ ultrapure water at 37 °C, pH 7.2) and the zinc concentration in the medium was analysed over time by total reflection X-ray fluorescence spectroscopy (TXRF S2 PicoFox, Bruker).

The reusability of the ZnO and ZnO–rGO functionalised surfaces was investigated by performing four consecutive cycles of bacterial exposure and UV irradiation on the same specimens. The tested samples were washed with PBS for 15 minutes and dried at 50 °C overnight after each run. In addition, both bacteria colonizing the surfaces and the film integrity were visualized by scanning electron microscopy (SEM, Zeiss DSM 950). The samples were prepared for observation by a fixation process with glutaraldehyde 5% (v/v) in 0.2 M sodium cacodylate buffer at pH 7.2. After fixing for 1 hour, the samples were washed in cacodylate buffer and dehydrated with ethanol and acetone.

### Statistical analysis

Statgraphics Centurion XVII software was used to perform a one- or two-way analysis of variance (ANOVA). Mean comparison was performed using Tukey's test ($p < 0.05$), while Grubbs' test was used to find the outliers following ASTM standard E178-00. In what follows, the results are presented as the average plus/minus standard deviation.

## Results and discussion

The X-ray diffraction patterns of the ZnO, rGO and ZnO–rGO functionalised surfaces are presented in Fig. 1. All the ZnO–rGO composite films exhibited similar diffraction patterns to the mono-component ZnO coating and corresponded to the hexagonal würtzite structure of zinc oxide (ICSD files 01-079-0206). The diffraction peaks at 31.8°, 34.4°, 36.3°, 47.5°, 56.6°, 62.9° and 68.0° can be indexed to the (100), (002), (101), (102), (110), (103) and (112) planes, respectively. rGO typically displays two diffraction peaks at 26° and 44.5° corresponding to the (002) and (100) stacked planes, respectively.[40] However, these peaks were not detected in the rGO and ZnO–rGO films, which might be due to the low rGO content and its relatively low diffraction intensity compared to ZnO in these composites.[11,41–43] On the other hand, the absence of these peaks could also indicate disorder and a high exfoliation degree of the rGO sheets (the absence of nanosheet stacking).[44]

Raman maps of the functionalised surfaces were acquired in order to further characterise the structure of the different phases in the composites. First, representative areas were selected by optical microscopy. Fig. 2a–c presents optical images of the

 

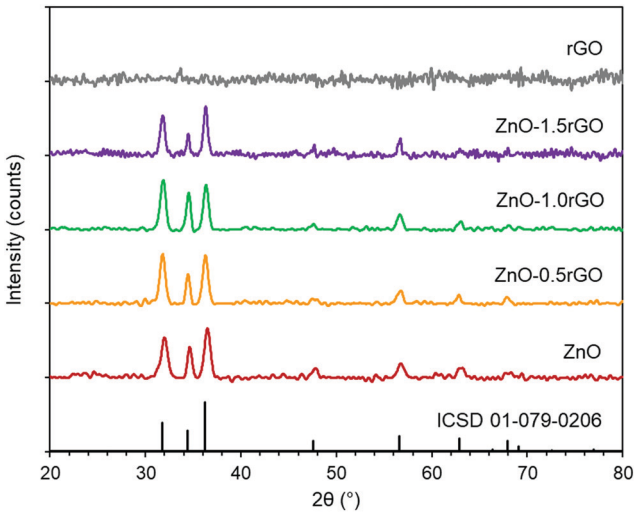


Fig. 1 X-ray diffraction patterns of ZnO ■, ZnO–0.5rGO ■, ZnO–1.0rGO ■, ZnO–1.5rGO ■, and rGO ■, functionalised surfaces.

ZnO, rGO and ZnO–1.0rGO coatings (the remaining films are shown in the ESI,† Fig. S1). It is clear that the increase in the rGO content led to an increase in the surface roughness of the nanocomposite films. Raman spectra of the ZnO–1.0rGO film were recorded by scanning the marked area. Fig. 2e and g show two of those Raman spectra from the selected zones, where ZnO and rGO were predominant, respectively. In Fig. 2e, the band at 473 $cm^{-1}$ corresponded to the E2 high frequency mode of the ZnO würtzite structure from the $C_{6v}$ ($P6_3mc$) space group.[45–47] The contribution at 578 $cm^{-1}$ is characteristic of structural defects in ZnO and was assigned to the $E_1$ (LO) mode. The small shoulder around 380 $cm^{-1}$ and a small contribution at 410 $cm^{-1}$ were attributed to the $A_1$ (TO) and $E_1$ (TO) mode frequencies, respectively.[45] The bands observed around 380 and 1145 $cm^{-1}$ were due to multiple scattering processes. Fig. 2g shows the characteristic D and G bands of the rGO phase in the nanocomposite at 1375 and 1604 $cm^{-1}$, respectively. The relative intensity of these graphene-associated bands, the $I_D/I_G$ ratio, varies from the initial precursor (GO, Fig. S2, ESI†) to the final composite, proving the achievement of GO reduction (rGO) during coating.[48–50]

Subsequent analysis by selecting the characteristic bands of each of the components (473 and 1375 $cm^{-1}$ for ZnO and rGO, respectively) allowed us to obtain the distribution maps on the surface (Fig. 2d and f for ZnO and rGO, respectively. The remaining films are shown in Fig. S3, ESI†). Both components were uniformly dispersed over the entire surface, although areas richer in one or the other component were appreciable. The rGO sheets seemed to be stacked onto the ZnO aggregates, displaying a greater proportion on the surface as the content in this component increased (Fig. S3, ESI†).

SEM and TEM experiments were conducted to investigate the morphology of the different phases in the ZnO and ZnO–rGO functionalised surfaces. Fig. 3a shows that in the absence

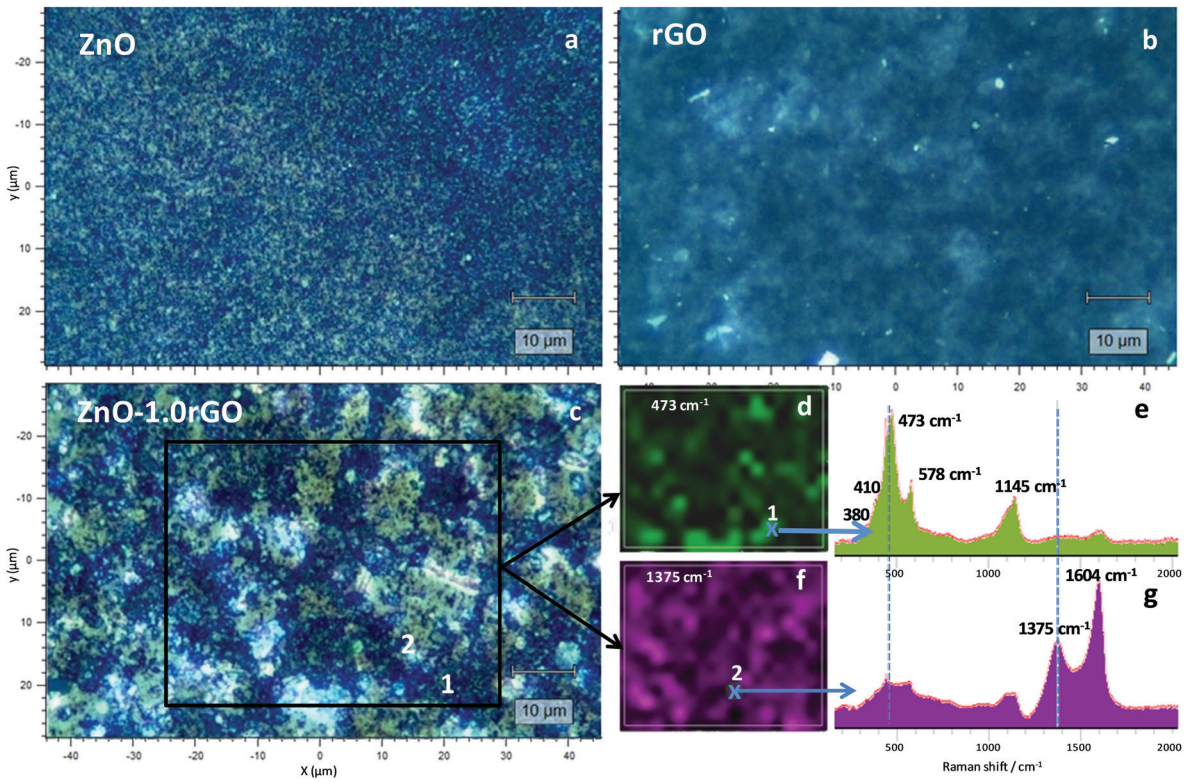


Fig. 2 Optical microscopy images (100× magnification) of the ZnO (a), rGO (b) and ZnO–1.0rGO (c) functionalised surfaces. Intensity colour maps of the Raman bands at 473 $cm^{-1}$ (d) and 1375 $cm^{-1}$ (f). Raman spectra corresponding to the points 1 (e) and 2 (g) of the c image. The black square in the c image indicates the Raman mapping area.

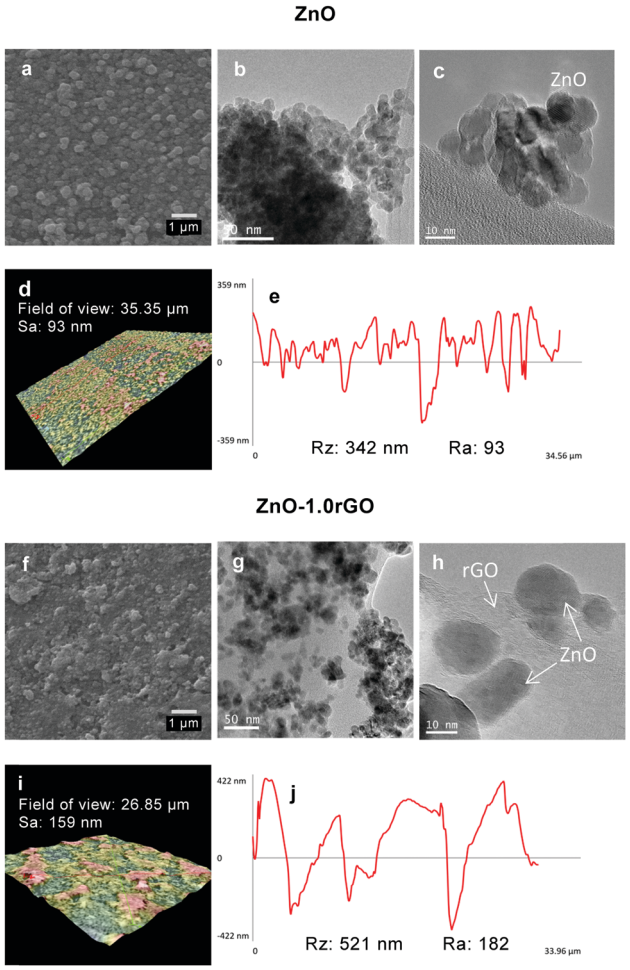


Fig. 3 SEM (a and f), TEM (b, c, g and h), 3D roughness reconstruction (d and i) and roughness profiles (e and j) of the ZnO and ZnO–1.0rGO photocatalytic surfaces.

of rGO, uniform ZnO films with 100–300 nm diameter aggregates were obtained. As shown in the SEM images of the composites (Fig. 3f and Fig. S4, ESI†), apart from the ZnO aggregates, larger islands scattered on the surface were observed and their proportion increased with the rGO content, conferring a greater surface roughness as it was already observed in the Raman images described above. These entities would correspond to the rGO sheets on the surface. The intimate interfacial contact between ZnO and rGO was further evidenced by TEM analysis, as presented in Fig. 3g and h. The TEM images of ZnO–rGO confirmed the formation of bi-dimensional rGO sheets without agglomeration. The preparation of composites is a way to avoid restacking of the GO sheets. These rGO sheets were decorated with ZnO nanoparticles with an average size of ~10 nm (see the particle size distribution in Fig. S5, ESI†). No differences in size were observed between ZnO nanoparticles prepared in the absence or the presence of rGO.

The surface topography of the ZnO and ZnO–1.0rGO photocatalytic films was characterised with 3D roughness reconstruction (Fig. 3d and i). Fig. 3e and j display a roughness profile of each of the investigated surfaces. The $S_a$ (arithmetical mean height of the surface, ISO 25178) values were 93 and 159 nm for the ZnO and ZnO–1.0rGO functionalised surfaces, respectively. Interestingly, the ZnO film presented a comparatively flat surface with slightly high deviations, which corresponded to an $R_a$ arithmetic mean deviation of the roughness profile, ISO 4287, of 93 nm. In contrast, the surface of the ZnO–1.0rGO nanocomposite film exhibited an $R_a$ of 180 nm due to large agglomerations and cavities. The $R_z$ (the maximum height of the roughness profile, ISO 4287) values were 342 and 521 nm for the ZnO and ZnO–1.0rGO photocatalytic coatings, respectively, which might correspond to the film thickness since gaps between aggregates were occasionally exhibited.

The optical properties of the ZnO and ZnO–rGO coatings were characterised by using UV-vis diffuse reflectance spectroscopy, as shown in Fig. 4a. All the photocatalysts exhibited ZnO characteristic absorption in the UV region of the spectra, which is due to the promotion of electrons from the valence band to the conduction band. The Kubelka–Munk function was used to determine the band-gap, considering ZnO as a direct band-gap semiconductor.[51,52] The direct band-gap energies were estimated to be 3.33, 3.31, 3.31 and 3.30 eV for ZnO, ZnO–0.5rGO, ZnO–1.0rGO and ZnO–1.5rGO, respectively. The presence of rGO does not modify the band-gap energies of the semiconductor as all the materials presented similar values to those of the bare ZnO.

Photoluminescence (PL) spectra (Fig. 4b) were analysed to investigate the recombination rate of the photo-generated electrons and holes in the photocatalytic coatings.[53] Both the ZnO and the ZnO–rGO photocatalytic surfaces showed a broad band of blue-green emission in the range of 400–580 nm. This emission originated from the recombination of the photo-generated holes with electrons trapped at oxygen vacancies in ZnO.[54,55] The PL intensity of the ZnO–rGO coatings significantly decreased with the increasing rGO content compared to that of the pristine ZnO, suggesting that the presence of rGO in the composites diminished the recombination of electron–hole pairs, prolonging their lifetimes.[56–58] The conduction band and the valence band of ZnO are −4.05 and −7.25 eV (*vs.* vacuum), respectively,[59,60] and the work function of rGO is −4.42 eV.[61,62] On the basis of this band diagram, the photogenerated electrons at ZnO can be transferred from the conduction band to the rGO sheets, hindering the recombination of electron–hole pairs and thus enhancing the photocatalytic activity.[63,64] This process seemed to be optimum for ZnO–1.0rGO. Higher content did not lead to a significant difference. It might be possible that excess rGO could also provide other recombination centres.[62,65]

The wettability of the ZnO, ZnO–rGO and rGO functionalised surfaces before and after UV exposure simulating Winter–Fall, L(+), and Summer–Spring, L(++), irradiation was characterised by WCA measurements (Table 1). The WCA on bare glass substrates was 65.0 ± 0.4°, which did not change upon UV irradiation. The ZnO photocatalytic films were hydrophilic, showing a WCA value of 49.4 ± 2.8°. The ZnO–rGO film wettability decreased along with the rGO concentration due to the rGO hydrophobic nature, showing WCA values of 59.9 ± 2.1°, 69.8 ± 1.8° and 95.5 ± 1.7° for ZnO–0.5rGO, ZnO–1.0rGO and ZnO–1.5rGO, respectively. However, the rGO functionalised

 

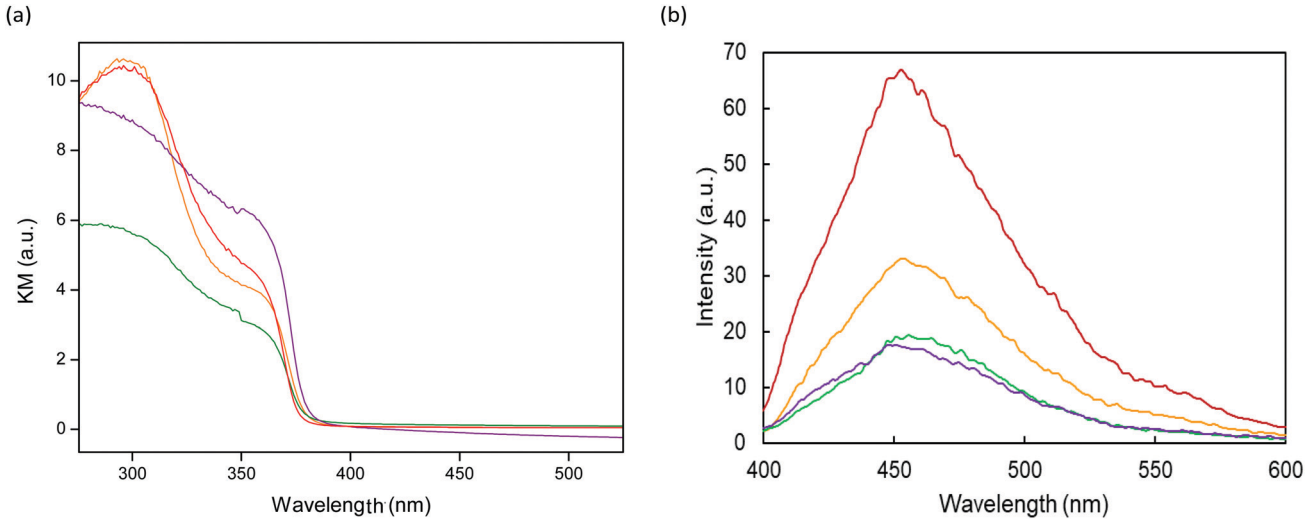


Fig. 4 UV-vis diffuse reflectance (a) and photoluminescence (PL) spectra at an excitation wavelength of 350 nm (b) for ZnO ■, ZnO–0.5rGO ■, ZnO–1.0rGO ■ and ZnO–1.5rGO ■ photocatalytic surfaces.

Table 1 WCA (°) measurements for non-functionalised (bare glass) and ZnO, ZnO–rGO and rGO functionalised surfaces

| | No irradiation L(−) | Winter irradiation L(+) | Summer irradiation L(++) |
|---|---|---|---|
| Bare glass | 65.0 ± 0.4 | 65.5 ± 2.8 | 64.2 ± 1.2 |
| ZnO | 49.4 ± 2.8 | 21.4 ± 3.3 | 12.6 ± 2.9 |
| ZnO–0.5rGO | 59.9 ± 2.1 | 45.0 ± 3.1 | 23.7 ± 1.5 |
| ZnO–1.0rGO | 69.8 ± 1.8 | 51.4 ± 3.2 | 33.5 ± 3.0 |
| ZnO–1.5rGO | 95.5 ± 1.7 | 64.7 ± 2.5 | 42.7 ± 3.8 |
| rGO | 32.8 ± 2.7 | 29.7 ± 1.9 | 28.8 ± 3.0 |

surfaces were hydrophilic with a WCA value of 32.8 ± 2.7° and they barely changed after UV irradiation. The hydrophilicity of the GO sheets can be modified using different strategies such as targeted surface functionalization, structural doping, *etc.* The interaction between both components in the composite during the synthesis can lead to certain modifications, in such a way that the properties of the final products differ from those of the isolated compounds. Both the ZnO and ZnO–rGO nanocomposite films exhibited photoinduced hydrophilicity under UV irradiation, increasing their wettability significantly upon L(+) daylight ($p < 0.05$) and becoming even more hydrophilic after L(++) irradiation ($p < 0.05$). Under UV irradiation, the photogenerated electron–hole pairs react with Zn–O lattice bonds, forming $Zn^+$ defective sites and oxygen vacancies, which cause water dissociative adsorption.[66–68]

The antimicrobial activity of the ZnO, rGO and ZnO–rGO functionalised surfaces was assayed by means of *S. aureus* aerosol exposure and quantifying CFU reduction (Fig. 5 and Table S1, ESI†). Both the ZnO and ZnO–rGO photocatalytic films exhibited >99% (>2-log) reduction in CFUs compared to the bare glass controls even in the absence of irradiation. Upon Winter–Fall irradiation, a significantly higher inhibition of bacterial growth was observed for all the photocatalytic surfaces tested ($p < 0.05$). When Summer–Spring irradiation was used, notable differences were observed between the ZnO and

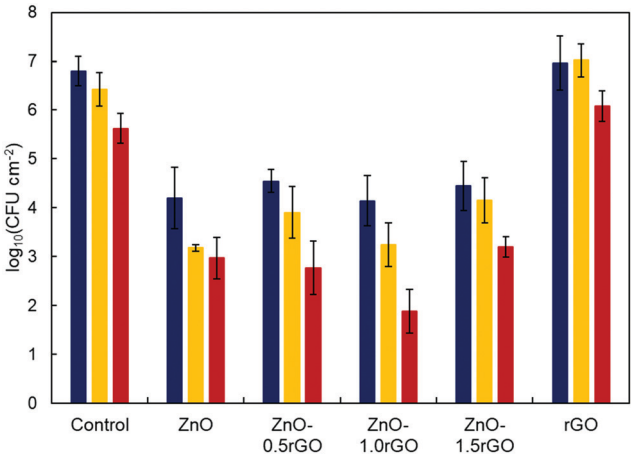


Fig. 5 Colony-forming units of *S. aureus* measured from the surface after bacteria-containing aerosol spraying on non-functionalised control, and ZnO, ZnO–rGO and rGO functionalised surfaces in the absence of irradiation [L(−), ■] and upon Winter–Fall [L(+), ■] and Summer–Spring [L(++), ■] irradiation.

ZnO–rGO photocatalytic coatings. In this case, the optimal loading amount of rGO on the ZnO–rGO nanocomposite film was 1 wt%, which was essentially free of viable bacteria, achieving up to ~5-log reduction. It is worth noting that such a high degree of disinfection was achieved within just a few minutes of illumination. On the other hand, rGO exhibited practically no bactericidal effect (Fig. 5 and Table S1, ESI†).

The live/dead and FilmTracer SYPRO Ruby biofilm matrix stain images of *S. aureus* on the ZnO–rGO photocatalytic surfaces were obtained in order to further investigate the influence of the rGO amount in the nanocomposite (Fig. 6 and Fig. S6, S7 in ESI†).

Live/dead staining revealed that the presence of the photocatalytic material remarkably decreased the number of viable green-stained cells compared to the non-functionalised or

rGO-functionalised surfaces. As the ZnO–rGO surfaces were irradiated and the UV exposure time was increased, more bacteria became yellowish or red-marked. Red fluorescence indicates membrane-damaged and non-viable bacteria, highlighting the biocide action of the photocatalysts. The increment of the rGO content from 0.5 to 1 wt% in the ZnO–rGO film caused a decrease in the cell viability, which then increased in the nanocomposite with 1.5 wt% rGO. FilmTracer SYPRO Ruby stain red-marks the protein matrix of extracellular polymeric substances (EPS) that embed the aggregates of bacterial cells forming a biofilm. Therefore, this test allows biofilm visualization. EPS enable bacteria to colonize the surfaces, providing them with a physical barrier and protection against environmental stress factors.[69,70] For bare surfaces, without coating (control), all the polymeric matrixes clearly appear marked in red by the stain both in the dark and under illuminated conditions (Fig. 6). Therefore, in the absence of the photocatalytic material, clear biofilm formation was detected. However, it was dramatically reduced on the ZnO–rGO coated surfaces, which resulted in the irradiated specimens being essentially free of the polymeric matrix, proving that the coatings present antibiofouling activity disrupting biofilm formation.

The formation of reactive oxygen species such as $O^{2\bullet-}$, HO$^\bullet$ and $H_2O_2$ is usually considered one of the main antibacterial mechanisms for ZnO and graphene-related materials.[71,72] Therefore, HTA (2-hydroxyterephthalic acid) fluorescence measurements were carried out to estimate the amount of HO$^\bullet$ radicals produced during the photocatalytic process on the functionalised surfaces and correlate this with their biocide response.[73–76]

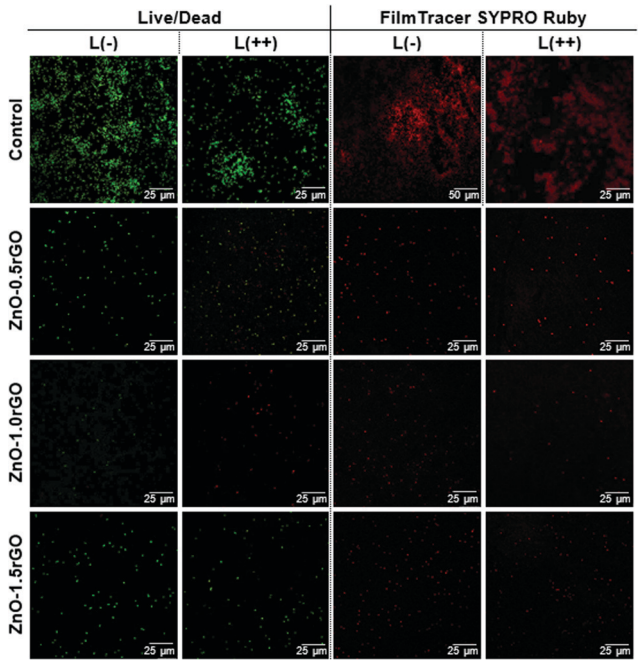


Fig. 6 Live/dead and FilmTracer SYPRO Ruby Biofilm Matrix Stain of *S. aureus* on non-functionalised (control) and ZnO–rGO functionalised surfaces in the absence of irradiation, L(–), and upon Summer–Spring irradiation, L(++).

Fig. 7 shows the HTA fluorescence intensity in the aqueous basic solution of TA. A significant increase in the relative fluorescence units (RFU) was observed with the increase of the UV irradiation time ($p < 0.05$), supporting HO$^\bullet$ radical generation at the photocatalyst–water interface. The addition of rGO favoured greater production of radicals up to a certain concentration; rGO content higher than 1 wt% no longer led to an improvement in the formation of these species. Therefore, HO$^\bullet$ formation on the ZnO–rGO photocatalytic films showed the same trend as that of the antimicrobial activity tests, resulting in the nanocomposite with 1 wt% rGO exhibiting both the highest HTA fluorescence intensity upon L(++) irradiation ($p < 0.05$) and the highest bactericidal effect.

The results suggest that the addition of an appropriate amount of rGO considerably enhanced the antimicrobial activity of ZnO. Among the ZnO–rGO coatings, 1 wt% rGO nanocomposites achieved the optimal synergistic interaction between ZnO and rGO. The improvement of the photocatalytic performance could be ascribed to the intimate interfacial contact and enhanced electronic interaction between ZnO nanoparticles and rGO sheets in the composite.[60] The photogenerated electrons in ZnO under UV irradiation can be accepted and transported by rGO due to its two-dimensional π-conjugation structure and superior electrical conductivity.[16,60,63,77] Therefore, rGO draws electrons from ZnO and the charge carrier separation decreases the recombination of the photogenerated electron–hole pairs, which was confirmed from the PL measurements. This allows the holes in ZnO and the electrons captured by rGO to be involved in the reaction with adsorbed water (or surface hydroxyl) and oxygen to form hydroxyl and superoxide radicals, respectively.[11] In this way, the photocatalytic activity and thus the antimicrobial performance of the ZnO–rGO nanocomposite film were improved compared to those of the pristine ZnO. The decreased activity at 1.5 wt% rGO loaded ZnO may be due to the fact that excess rGO increases the absorbance and scattering of

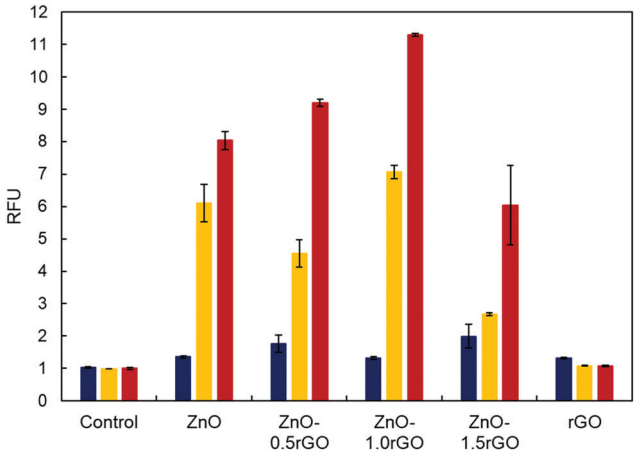


Fig. 7 Relative fluorescence units (RFUs) of HTA due to HO$^\bullet$ production in the liquid in contact with non-functionalised (control) and ZnO, ZnO–rGO and rGO functionalised surfaces in the absence of irradiation [L(–), ■], and upon Winter–Fall [L(+), ■] and Summer–Spring [L(++), ■] irradiation.

photons and can form recombination centres.[17,62,65,78] GO and rGO can exert a bactericidal effect upon physical damage of the cell membrane by sharp graphene nanosheets.[79,80] In this work, the functionalised surfaces with only an rGO component did not exhibit antimicrobial activity probably because the rGO sheets could be more agglomerated in the absence of ZnO or present rounded edges (Fig. S4, ESI†). The ZnO and ZnO–rGO films exhibited some antimicrobial activity compared with the bare glass substrates or the rGO-functionalised surfaces even in the dark. The main antibacterial mechanism of ZnO in the dark has been ascribed to the leaching of $Zn^{2+}$ ions, which are internalized by the cell damaging different cellular components.[9,81–83] In order to evaluate the possible existence of this mechanism in our systems, the concentration of $Zn^{2+}$ released from the ZnO and ZnO–1.0rGO photocatalytic coatings into Milli-Q water at 37 °C was measured (Fig. S8, ESI†). The $Zn^{2+}$ concentration remained approximately constant after 10 hours, reaching a value of 6 μg $cm^{-2}$ or 2.5 mg $L^{-1}$. This value was well below its solubility limit,[84] confirming the high stability achieved by our films in an aqueous medium. The presence of $Zn^{2+}$ ions, although low, could contribute to the activity observed in the dark compared to the control. On the other hand, the higher hydrophobicity conferred by rGO could also inhibit bacterial adhesion to these photocatalytic surfaces, thus hindering their colonization.

Both photogenerated ROS and bioavailable dissolved zinc have been shown to penetrate cells and damage cellular components through oxidative stress.[85,86] Here, intracellular oxidative stress was assessed using DCF as an indicator (see the experimental part). Fig. 8 shows the DCF fluorescence intensity on 1.065 × 1.065 $cm^2$ non-functionalised surfaces and ZnO and ZnO–1.0rGO functionalised surfaces. The higher fluorescence intensity of the ZnO–1.0rGO photocatalytic films compared to that of the ZnO ones indicates that the presence of rGO sheets in the composite increases the intracellular oxidative stress markedly. In addition, the difference increased considerably when the UV exposure time increased (from 3 to 6 minutes). This result is consistent with those observed during the experiments of CFU and $HO^{\bullet}$ quantification. Therefore, taking into account the stability against Zn leaching, the results indicate that the ZnO–rGO functionalised coating impaired the bacterial cells due to cell membrane damage and a high degree of intracellular oxidative stress was produced by the photogenerated reactive oxygen species that were promoted by the presence of rGO.

The reusability and stability of the photocatalytic films were investigated by performing cyclic experiments of the ZnO and ZnO–1.0rGO functionalised surfaces (Fig. 9). With the increase of the recycle number, ZnO exhibited a clear decrease in the antimicrobial activity even under UV irradiation (Fig. 9b). After three cycles, the differences between the ZnO-functionalised surfaces and the controls were not significant ($p > 0.05$ for growth inhibition). In contrast, the antimicrobial performance of the ZnO–1.0rGO nanocomposite film almost remained

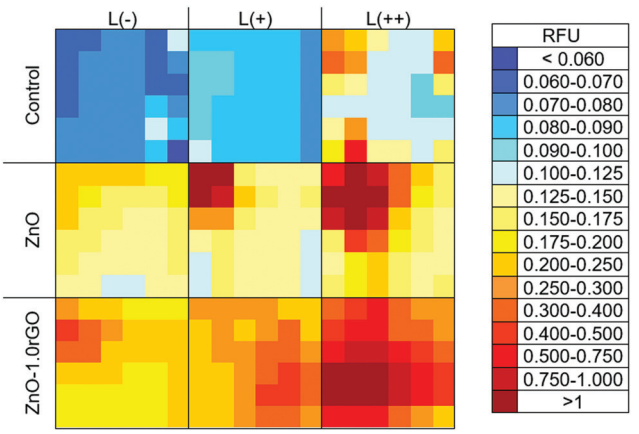


Fig. 8 Relative fluorescence units (RFUs) of intracellular DCF due to ROS production on non-functionalised surfaces (control), ZnO and ZnO–1.0rGO functionalised surfaces (1.065 × 1.065 $cm^2$, with 1.775 mm step size) in the absence of irradiation, L(−), and upon Winter–Fall, L(+), and Summer–Spring, L(++), irradiation.

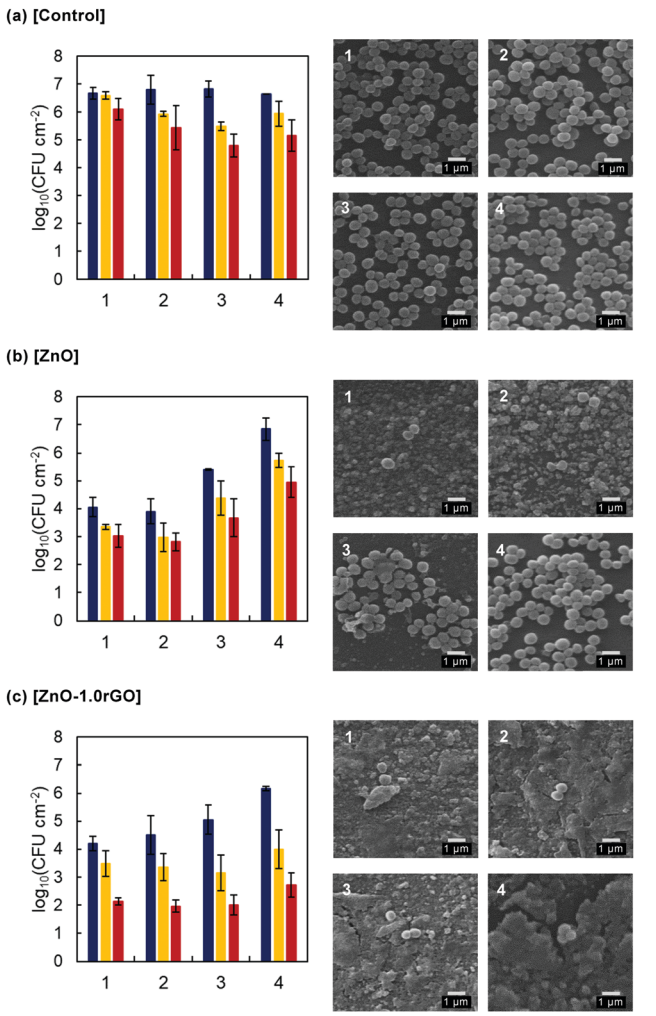


Fig. 9 Colony-forming units (CFUs) and SEM images [L(++),] of *S. aureus* on non-functionalised surfaces (a) and ZnO (b) and ZnO–1.0rGO (c) functionalised surfaces in the absence of irradiation [L(−), ], and upon Winter–Fall [L(+), ] and Summer–Spring [L(++), ] irradiation for four consecutive cycles.

constant along the four cycles under both irradiation conditions, winter–fall and summer–spring (Fig. 9c). The activity decrease observed in the dark after the fourth cycle could be due to the increased surface roughness visualized in the SEM images (Fig. 9c, 1–4); the modification of the textural properties could favour a higher colonization of the surface but the high photoactivity of the material retained the bactericidal action on lighting.

As displayed in the SEM images of the non-functionalised surfaces, numerous unaltered bacterial cells with a round shaped morphology and a smooth surface were observed, reflecting easy bacterial colonization in the absence of coating. However, on the ZnO and ZnO–1.0rGO photocatalytic coatings the number of *S. aureus* cells noticeably decreased and clear bacterial shape alterations were visible. But along the cycles, differences were observed between the two types of coatings. ZnO-functionalised surfaces underwent extreme mass loss with the increase in cycles. In contrast, the morphology of the ZnO–1.0rGO film remained nearly the same even after reusing four times. Only some cracks were observed (Fig. S9, ESI†). All these data point to a protective role played by rGO, which would act as a shield preventing ZnO dissolution and then mass loss which consequently leads to a decrease in the bacterial efficiency.

These results demonstrate that the combination of ZnO nanoparticles with rGO sheets not only decreased the electron–hole pair recombination and enhanced the antimicrobial performance, but also significantly improved the lifetime of photocatalytic coatings. These data also reveal the importance of carrying out durability tests, since good performance must also include resistance and reuse after coating washing. Therefore, these ZnO–rGO nanocomposite films may represent a promising approach to reduce microbial growth on surfaces with different application fields.

## Conclusions

ZnO–rGO nanocomposite films with different weight ratios of rGO were synthesized by a sol–gel spin-coating technique. ZnO-functionalised surfaces were formed by aggregates of 100 to 300 nm consisting of 10–15 nm nanoparticles of ZnO with a würtzite structure, with $\sim 0.11 \pm 0.05$ mg cm$^{-2}$ of mass loading. The formation of thin rGO sheets decorated with ZnO nanoparticles ($\sim$15 nm) was confirmed by TEM analysis. The fabricated coatings exhibited less wettability along with the rGO concentration.

ZnO–rGO exhibited a strong antibacterial effect against the growth of a Gram-positive bacterium *S. aureus*. 1 wt% rGO nanocomposite coatings showed the highest antimicrobial activity, with up to $\sim$5-log reduction in the bacterial colony forming units just by exposing to daylight for 6 minutes (under 365 nm irradiation simulating Summer–Spring conditions). The enhancement of the bactericidal performance upon rGO addition was due to the effective reduction of photogenerated electron–hole pair recombination and is correlated with higher generation of HO$^{\bullet}$ radicals. Cell membrane damage and intracellular oxidative stress were attributed mainly to the photogenerated ROS. The ZnO–rGO composites displayed lower $Zn^{2+}$ leaching and considerably increased ROS generation compared to ZnO films alone. Moreover, the ZnO–rGO coated surfaces inhibited biofilm formation, as revealed by FilmTracer SYPRO Ruby staining.

Reusability tests showed that the lifetime of the ZnO-functionalised surfaces was significantly enhanced with the incorporation of rGO, which was attributed to the intimate interfacial interaction between ZnO nanoparticles and rGO sheets in the composite which stabilizes ZnO, preventing ZnO mass loss.

The great antibacterial activity and the recyclability demonstrated the potential use of ZnO–rGO photocatalytic coatings for surface antimicrobial functionalisation in a wide range of applications.

## Conflicts of interest

There are no conflicts to declare.

## Acknowledgements

This work has been supported by the Fundación Ramón Areces (OTR02666-20172353), the Regional Government of Madrid and the European Structural Funds (FoToArt project S2018/NMT-4367). LV thanks the Spanish Ministry of Education for her FPU grant (FPU17/03096). The authors are also grateful to ICTS "NANBIOSIS" for its Confocal Microscopy Service, to the Spanish MCIU/FEDER for funding the project EQC2018-004839-P to acquire the Raman equipment and to Prof. M. A. Bañares for providing its access.

## References

1 A. Gupta, S. Mumtaz, C.-H. Li, I. Hussain and V. M. Rotello, *Chem. Soc. Rev.*, 2019, **48**, 415–427.
2 D. M. Morens, G. K. Folkers and A. S. Fauci, *Nature*, 2004, **430**, 242–249.
3 O. Sánchez, *J. Membr. Sci.*, 2018, **545**, 240–249.
4 Y. Liu, L. Shi, L. Su, H. C. van der Mei, P. C. Jutte, Y. Ren and H. J. Busscher, *Chem. Soc. Rev.*, 2019, **48**, 428–446.
5 V. K. Yemmireddy and Y.-C. Hung, *Compr. Rev. Food Sci. Food Saf.*, 2017, **16**, 617–631.
6 A. Iglesias-Juez, F. Viñes, O. Lamiel-García, M. Fernández-García and F. Illas, *J. Mater. Chem. A*, 2015, **3**, 8782–8792.
7 A. Janotti and C. G. Van de Walle, *Rep. Prog. Phys.*, 2009, **72**, 126501.
8 E. de Lucas-Gil, P. Leret, M. Monte-Serrano, J. J. Reinosa, E. Enríquez, A. Del Campo, M. Cañete, J. Menéndez, J. F. Fernández and F. Rubio-Marcos, *ACS Appl. Nano Mater.*, 2018, **1**, 3214–3225.
9 M. Li, L. Zhu and D. Lin, *Environ. Sci. Technol.*, 2011, **45**, 1977–1983.
10 A. Ray Chowdhuri, S. Tripathy, S. Chandra, S. Roy and S. K. Sahu, *RSC Adv.*, 2015, **5**, 49420–49428.

 

11 H. Moussa, E. Girot, K. Mozet, H. Alem, G. Medjahdi and R. Schneider, *Appl. Catal., B*, 2016, **185**, 11–21.
12 J. Liu, M. D. Rojas-Andrade, G. Chata, Y. Peng, G. Roseman, J.-E. Lu, G. L. Millhauser, C. Saltikov and S. Chen, *Nanoscale*, 2018, **10**, 158–166.
13 J. C. Meyer, A. K. Geim, M. I. Katsnelson, K. S. Novoselov, T. J. Booth and S. Roth, *Nature*, 2007, **446**, 60–63.
14 S. Stankovich, D. A. Dikin, G. H. B. Dommett, K. M. Kohlhaas, E. J. Zimney, E. A. Stach, R. D. Piner, S. T. Nguyen and R. S. Ruoff, *Nature*, 2006, **442**, 282–286.
15 Y. H. Ng, A. Iwase, N. J. Bell, A. Kudo and R. Amal, *Catal. Today*, 2011, **164**, 353–357.
16 Q. Xiang, J. Yu and M. Jaroniec, *Chem. Soc. Rev.*, 2012, **41**, 782–796.
17 T. Xu, L. Zhang, H. Cheng and Y. Zhu, *Appl. Catal., B*, 2011, **101**, 382–387.
18 B. Xue and Y. Zou, *Appl. Surf. Sci.*, 2018, **440**, 1123–1129.
19 W. Han, L. Ren, X. Qi, Y. Liu, X. Wei, Z. Huang and J. Zhong, *Appl. Surf. Sci.*, 2014, **299**, 12–18.
20 S. Stankovich, D. A. Dikin, R. D. Piner, K. A. Kohlhaas, A. Kleinhammes, Y. Jia, Y. Wu, S. T. Nguyen and R. S. Ruoff, *Carbon*, 2007, **45**, 1558–1565.
21 W. Wang, J. Yu, Q. Xiang and B. Cheng, *Appl. Catal., B*, 2012, **119–120**, 109–116.
22 D. Xu, B. Cheng, S. Cao and J. Yu, *Appl. Catal., B*, 2015, **164**, 380–388.
23 N. Zhang, M.-Q. Yang, Z.-R. Tang and Y.-J. Xu, *ACS Nano*, 2014, **8**, 623–633.
24 Y. Zhang, Z.-R. Tang, X. Fu and Y.-J. Xu, *ACS Nano*, 2011, **5**, 7426–7435.
25 Q. Tan, X. Kong, X. Guan, C. Wang and B. Xu, *CrystEngComm*, 2020, **22**, 320–329.
26 Q. Tan, Z. Kong, X. Guan, L. Y. Zhang, Z. Jiao, H. C. Chen, G. Wu and B. Xu, *J. Colloid Interface Sci.*, 2019, **548**, 233–243.
27 C. G. Granqvist, *Sol. Energy Mater. Solar Cells*, 2012, **99**, 1–13.
28 M. Ikawa, T. Yamada, H. Matsui, H. Minemawari, J.y. Tsutsumi, Y. Horii, M. Chikamatsu, R. Azumi, R. Kumai and T. Hasegawa, *Nat. Commun.*, 2012, **3**, 1176.
29 N. Sahu, B. Parija and S. Panigrahi, *Indian J. Phys.*, 2009, **83**, 493–502.
30 R. Nisticò, D. Scalarone and G. Magnacca, *Microporous Mesoporous Mater.*, 2017, **248**, 18–29.
31 A. Uzum, K. Fukatsu, H. Kanda, Y. Kimura, K. Tanimoto, S. Yoshinaga, Y. Jiang, Y. Ishikawa, Y. Uraoka and S. Ito, *Nanoscale Res. Lett.*, 2014, **9**, 659.
32 S. Ahmadi, N. Asim, M. Alghoul, F. Hammadi, K. Saeedfar, N. Ludin, S. Zaidi and K. Sopian, *J. Photoenergy*, 2014, 19.
33 L. Spanhel and M. A. Anderson, *J. Am. Chem. Soc.*, 1991, **113**, 2826–2833.
34 L. Valenzuela, A. Iglesias, M. Faraldos, A. Bahamonde and R. Rosal, *J. Hazard. Mater.*, 2019, **369**, 665–673.
35 OIML, *The Scale of relative humidity of air certified against saturated salt solutions, International Recommendation*. Organisation Internationale de Métrologie Légale, Paris, 1996.
36 K.-i. Ishibashi, A. Fujishima, T. Watanabe and K. Hashimoto, *Electrochem. Commun.*, 2000, **2**, 207–210.
37 Y. Nosaka and A. Y. Nosaka, *Chem. Rev.*, 2017, **117**, 11302–11336.
38 A. Gomes, E. Fernandes and J. L. F. C. Lima, *J. Biochem. Biophys. Methods*, 2005, **65**, 45–80.
39 B. Kalyanaraman, V. Darley-Usmar, K. J. A. Davies, P. A. Dennery, H. J. Forman, M. B. Grisham, G. E. Mann, K. Moore, L. J. Roberts and H. Ischiropoulos, *Free Radic. Biol. Med.*, 2012, **52**, 1–6.
40 L. Tang, Y. Wang, Y. Li, H. Feng, J. Lu and J. Li, *Adv. Funct. Mater.*, 2009, **19**, 2782–2789.
41 D. Li, M. B. Müller, S. Gilje, R. B. Kaner and G. G. Wallace, *Nat. Nanotechnol.*, 2008, **3**, 101–105.
42 X. Liu, L. Pan, Q. Zhao, T. Lv, G. Zhu, T. Chen, T. Lu, Z. Sun and C. Sun, *Chem. Eng. J.*, 2012, **183**, 238–243.
43 H. Zhang, X. Lv, Y. Li, Y. Wang and J. Li, *ACS Nano*, 2010, **4**, 380–386.
44 R. K. Goyal, *Nanomaterials and nanocomposites: synthesis, properties, characterization techniques, and applications*, 1st edn, CRC Press, Boca Raton, 2017.
45 R. Cuscó, E. Alarcón-Lladó, J. Ibáñez, L. Artús, J. Jiménez, B. Wang and M. J. Callahan, *Phys. Rev. B: Condens. Matter Mater. Phys.*, 2007, **75**, 165202.
46 A. Umar, B.-K. Kim, J.-J. Kim and Y. B. Hahn, *Nanotechnology*, 2007, **18**, 175606.
47 R. Zhang, P.-G. Yin, N. Wang and L. Guo, *Solid State Sci.*, 2009, **11**, 865–869.
48 E. Asedegbega-Nieto, M. Perez-Cadenas, M. V. Morales, B. Bachiller-Baeza, E. Gallegos-Suarez, I. Rodriguez-Ramos and A. Guerrero-Ruiz, *Diamond Relat. Mater.*, 2014, **44**, 26–32.
49 A. Kaniyoor, T. T. Baby and S. Ramaprabhu, *J. Mater. Chem.*, 2010, **20**, 8467–8469.
50 H.-B. Zhang, J.-W. Wang, Q. Yan, W.-G. Zheng, C. Chen and Z.-Z. Yu, *J. Mater. Chem.*, 2011, **21**, 5392–5397.
51 X. Chen, S. Shen, L. Guo and S. S. Mao, *Chem. Rev.*, 2010, **110**, 6503–6570.
52 E. M. Patterson, C. E. Shelden and B. H. Stockton, *Appl. Opt.*, 1977, **16**, 729–732.
53 N. Zhang, Y. Zhang, M.-Q. Yang, Z.-R. Tang and Y.-J. Xu, *J. Catal.*, 2013, **299**, 210–221.
54 P. Kumbhakar, A. Pramanik, S. Biswas, A. K. Kole, R. Sarkar and P. Kumbhakar, *J. Hazard. Mater.*, 2018, **360**, 193–203.
55 B. Weng, M.-Q. Yang, N. Zhang and Y.-J. Xu, *J. Mater. Chem. A*, 2014, **2**, 9380–9389.
56 U. Alam, A. Khan, W. Raza, A. Khan, D. Bahnemann and M. Muneer, *Catal. Today*, 2017, **284**, 169–178.
57 J. Liqiang, Q. Yichun, W. Baiqi, L. Shudan, J. Baojiang, Y. Libin, F. Wei, F. Honggang and S. Jiazhong, *Sol. Energy Mater. Solar Cells*, 2006, **90**, 1773–1787.
58 H. N. Tien, V. H. Luan, L. T. Hoa, N. T. Khoa, S. H. Hahn, J. S. Chung, E. W. Shin and S. H. Hur, *Chem. Eng. J.*, 2013, **229**, 126–133.
59 M. Azarang, A. Shuhaimi, R. Yousefi and S. P. Jahromi, *RSC Adv.*, 2015, **5**, 21888–21896.
60 B. Li and H. Cao, *J. Mater. Chem.*, 2011, **21**, 3346–3349.
61 Y. Wu, M. Xu, X. Chen, S. Yang, H. Wu, J. Pan and X. Xiong, *Nanoscale*, 2016, **8**, 440–450.

62 N. Yang, J. Zhai, D. Wang, Y. Chen and L. Jiang, *ACS Nano*, 2010, **4**, 887–894.
63 M.-Q. Yang and Y.-J. Xu, *Phys. Chem. Chem. Phys.*, 2013, **15**, 19102–19118.
64 N. Zhang, Y. Zhang and Y.-J. Xu, *Nanoscale*, 2012, **4**, 5792–5813.
65 M. Ahmad, E. Ahmed, Z. L. Hong, J. F. Xu, N. R. Khalid, A. Elhissi and W. Ahmed, *Appl. Surf. Sci.*, 2013, **274**, 273–281.
66 S. Karuppuchamy and S. Ito, *Vacuum*, 2008, **82**, 547–550.
67 V. Khranovskyy, T. Ekblad, R. Yakimova and L. Hultman, *Appl. Surf. Sci.*, 2012, **258**, 8146–8152.
68 R.-D. Sun, A. Nakajima, A. Fujishima, T. Watanabe and K. Hashimoto, *J. Phys. Chem. B*, 2001, **105**, 1984–1990.
69 S. Fulaz, S. Vitale, L. Quinn and E. Casey, *Trends Microbiol.*, 2019, **27**, 915–926.
70 P. P. Mahamuni-Badiger, P. M. Patil, M. V. Badiger, P. R. Patel, B. S. Thorat-Gadgil, A. Pandit and R. A. Bohara, *Mater. Sci. Eng., C*, 2020, **108**, 110319.
71 G. Applerot, A. Lipovsky, R. Dror, N. Perkas, Y. Nitzan, R. Lubart and A. Gedanken, *Adv. Funct. Mater.*, 2009, **19**, 842–852.
72 S. Liu, T. H. Zeng, M. Hofmann, E. Burcombe, J. Wei, R. Jiang, J. Kong and Y. Chen, *ACS Nano*, 2011, **5**, 6971–6980.
73 U. Alam, T. A. Shah, A. Khan and M. Muneer, *Sep. Purif. Technol.*, 2019, **212**, 427–437.
74 H. Bozetine, Q. Wang, A. Barras, M. Li, T. Hadjersi, S. Szunerits and R. Boukherroub, *J. Colloid Interface Sci.*, 2016, **465**, 286–294.
75 S.-M. Lam, J.-C. Sin, A. Z. Abdullah and A. R. Mohamed, *J. Colloid Interface Sci.*, 2015, **450**, 34–44.
76 X. Xu, Y. Jia, L. Xiao and Z. Wu, *Chemosphere*, 2018, **193**, 1143–1148.
77 C. Zhu, S. Guo, P. Wang, L. Xing, Y. Fang, Y. Zhai and S. Dong, *Chem. Commun.*, 2010, **46**, 7148–7150.
78 X. Wu, L. Wen, K. Lv, K. Deng, D. Tang, H. Ye, D. Du, S. Liu and M. Li, *Appl. Surf. Sci.*, 2015, **358**, 130–136.
79 O. Akhavan and E. Ghaderi, *ACS Nano*, 2010, **4**, 5731–5736.
80 F. Zou, H. Zhou, D. Y. Jeong, J. Kwon, S. U. Eom, T. J. Park, S. W. Hong and J. Lee, *ACS Appl. Mater. Interfaces*, 2017, **9**, 1343–1351.
81 B. A. Holt, S. A. Gregory, T. Sulchek, S. Yee and M. D. Losego, *ACS Appl. Mater. Interfaces*, 2018, **10**, 7709–7716.
82 J. Pasquet, Y. Chevalier, J. Pelletier, E. Couval, D. Bouvier and M.-A. Bolzinger, *Colloids Surf., A*, 2014, **457**, 263–274.
83 M. Premanathan, K. Karthikeyan, K. Jeyasubramanian and G. Manivannan, *Nanomedicine*, 2011, **7**, 184–192.
84 C. A. David, J. Galceran, C. Rey-Castro, J. Puy, E. Companys, J. Salvador, J. Monné, R. Wallace and A. Vakourov, *J. Phys. Chem. C*, 2012, **116**, 11758–11767.
85 A. Sirelkhatim, S. Mahmud, A. Seeni, N. H. M. Kaus, L. C. Ann, S. K. M. Bakhori, H. Hasan and D. Mohamad, *Nano-Micro Lett.*, 2015, **7**, 219–242.
86 W. Song, J. Zhang, J. Guo, J. Zhang, F. Ding, L. Li and Z. Sun, *Toxicol. Lett.*, 2010, **199**, 389–397.